MDPI

Article

The Tribo-Corrosion Behavior of Monel 400 Alloy in Marine Environment at Varied Rotational Velocities

Yuhua Zhu [1,2], Jianzhang Wang [1,*], Hao Liu [1] and Fengyuan Yan [1,*]

[1] State Key Laboratory of Solid Lubrication, Lanzhou Institute of Chemical Physics, Chinese Academy of Sciences, Lanzhou 730000, China
[2] Center of Materials Science and Optoelectronics Engineering, University of Chinese Academy of Sciences, Beijing 100049, China
[*] Correspondence: wangjz@licp.cas.cn (J.W.); fyyan@licp.cas.cn (F.Y.)

Abstract: Monel 400 alloy is widely employed in marine engineering equipment due to its excellent corrosion resistance, high strength and toughness. In this paper, the tribo-corrosion behavior of Monel 400 alloy in seawater under different rotational velocities was investigated by a pin-disk tribometer with an integrated electrochemical cell. The results revealed that the material loss rate and friction coefficient of the Monel 400 alloy, after tribo-corrosion and mechanical wear tests, increased with increasing rotational velocity. Under mechanical-wear conditions, the material loss rate increased with the sliding distance extension at higher velocities, and then more serious crack nucleation and propagation occurred at the subsurface. Under tribo-corrosion conditions, when the rotational velocities increased from 0.125 m/s to 0.5 m/s, the thickness of the corrosion product's layer was reduced from 50 nm to 30 nm; that is, the lubrication of the corrosion product became worse. As a result, the material-loss rate and friction coefficient increased significantly at the velocity of 0.5 m/s. Importantly, the antagonistic effect, rather than the synergistic effect, between corrosion and mechanical wear, has been verified for the tribo-corrosion of Monel 400 alloy in seawater, and the mechanism was analyzed.

Keywords: Monel 400 alloy; antagonistic effect; corrosion product; sliding distance; crack nucleation

1. Introduction

Recently, there has been an increasing demand for friction parts with high performance to serve in marine engineering [1–3]. Among various metallic materials, Ni-Cu alloys are more frequently used for marine applications due to their excellent corrosion resistance [4,5]. However, the characteristics of poor lubricity and strong corrosivity of seawater usually lead to serious tribo-corrosion problems.

For marine equipment, the working condition parameters of different friction pairs are different, including load, velocity and movement mode. Among them, velocity is one of the key parameters for the normal operation of friction components, which has a great influence on the tribological behavior of materials [6–9]. Over the past 30 years, much effort has been made regarding the influence of rotational velocity in corrosive environments [10–13]. Generally, the material loss of the alloy after the tribo-corrosion process is larger than the additive material loss of mechanical wear and corrosion acting independently [14,15]. The corrosion–wear interaction contributes a nonnegligible component to the total material loss [16,17]. Under such conditions, the impact mechanism of rotational velocity on the tribo-corrosion behavior of alloy is mainly divided into two aspects, including the repassivation rate for the damaged surface and subsurface deformation [18]. The wear rate of the Ni-17.5Si-29.3Cr alloy in H_2SO_4 solution increases with the rotational velocities increasing, due to crack initiation and propagation [19]. A similar growing trend is also determined in titanium alloy in a Ringer solution, where, at the highest rotational velocity, the material loss and synergistic factor are the highest [20].

Among Ni-Cu alloys, Monel 400 alloy is widely employed in marine engineering due to its excellent corrosion resistance, good strength and toughness. Our previous studies have explored the influence of applied load and potential on its tribo-corrosion behavior [21,22]. As a single-phased Ni-Cu alloy, Monel 400 alloy exhibits a unique interaction between wear and corrosion. An abnormal antagonistic effect of corrosion on mechanical wear is found, which is highly related to the lubricating performance of the nano-spherical corrosion product which is only generated in tribo-corrosion conditions. However, for the Monel 400 alloy, the influence mechanism of rotational velocity on tribo-corrosion behavior and the resultant change in microstructure under the dual action of corrosion and mechanical wear remain unclear.

In this study, the influence of rotational velocity on the tribo-corrosion behavior of Monel 400 alloy was studied. The quantitative calculation was used to evaluate the interaction of corrosion and mechanical wear of the Monel 400 alloy. Special attention was focused on the formation of the corrosion product's layer at the surface and the microstructure evolution at the subsurface of the Monel 400 alloy.

2. Experiment

2.1. Materials

The chemical component (wt%) of Monel 400 alloy is placed in Table 1, which was purchased from Shaanxi Qingye Special Materials Co., Ltd. (Xi'an, China). The counterpart Al_2O_3 pin was provided by Dehe Special Porcelain Factory (Zhejiang, China). The corrosion medium is artificial seawater, prepared according to **ASTM D1141-98**. The pH value was adjusted to 8.2 using 0.1 mol/L NaOH solution. The chemical compositions are listed in Table 2.

Table 1. Chemical components of the Monel 400 alloy.

Element	Cu	Fe	Mn	Si	C	S	P	Ni
Content (wt.%)	29.65	1.85	1.09	0.22	0.08	0.003	0.003	Bal.

Table 2. The chemical compositions of seawater.

Components	Concentration (g/L)
NaCl	24.53
$MgCl_2$	5.20
Na_2SO_4	4.09
$CaCl_2$	1.16
KCl	0.695
$NaHCO_3$	0.201
KBr	0.101
$SrCl_2$	0.025
H_3BO_3	0.027
NaF	0.003

Before wear tests, the specimens of Monel 400 alloy were machined into annular shapes with an external diameter of 54 mm, internal diameter of 38 mm and height of 13 mm. The sliding surfaces of all specimens were polished by 800 mesh SiC sandpaper and ultrasonically washed with ethanol. After that, the other surfaces of the specimens were covered with insulating paint to avoid corrosion expect for the sliding surfaces. The size of Al_2O_3 counterpart was Φ 4.6 × 15 mm, and the working surface was in spherical form with a radius of 4.75 mm.

2.2. Tribo-Corrosion Measurement

To monitor the electrochemical signal of Monel 400 alloy during sliding *in situ*, a modified MMW-1 pin-on-disk wear device equipped with a PARTAT 3000A electrochemical

workstation (Ametek, Bowen, PA, USA) was used. A three-electrode system was employed to collect electrochemical signal, using a Monel 400 ring as the working electrode, a Pt gauze as the counter electrode and an Ag/AgCl electrode as the reference electrode.

Both tribo-corrosion and mechanical wear tests were performed at 75 N for 60 min under rotational velocities ranging from 0.125 m/s to 0.5 m/s. For tribo-corrosion tests, the open circuit potential was monitored before sliding for 20 min, during sliding for 60 min and after sliding for another 20 min. The mechanical wear test was conducted with an applied potential of −0.9 V to inhibit electrochemical corrosion, and the specimens were immersed in seawater before and after sliding for 20 min, respectively. The dynamic polarization tests were measured with a scan rate of 10 mV/s from −0.7 V to −1210.2 V under static corrosion and tribo-corrosion tests, respectively.

2.3. Characterization

A JEM−5600LV scanning electron microscope (SEM) (JSM-5601LV, Japan Electron Optics Laboratory, Akishima, Japan) was utilized to observe the morphology of the damaged surface and subsurface of the Monel 400 alloy. X-ray photoelectron spectroscopy with an Al Kα X-ray source (Thermo Scientific, Waltham, MA, USA) was employed to analyze the chemical composition of the corrosion product. The binding energy was calibrated by the C1s peak binding energy at 284.8 eV. To study the microstructure evolution underneath the damaged surface, a Helios G4 UX Focus Ion Beam (FIB) was used to take samples from the sliding surface, and a thin membrane was prepared, which was observed by a Tecnai G2S-Twin F20 transmission electron microscope (TEM) (FEI, Lexington, KY, USA).

3. Results

3.1. Microstructure of Monel 400 Alloy

The TEM morphology and selected-area electron diffraction (SAED) pattern of the pristine Monel 400 alloy are shown in Figure 1. From Figure 1a, the equiaxed grains (~50 nm) were observed. Figure 1b exhibits regular two-dimensional diffraction spots, which are consistent with the diffraction pattern of the single-phased Monel 400 alloy in the face-centered cubic (FCC) crystalline structure.
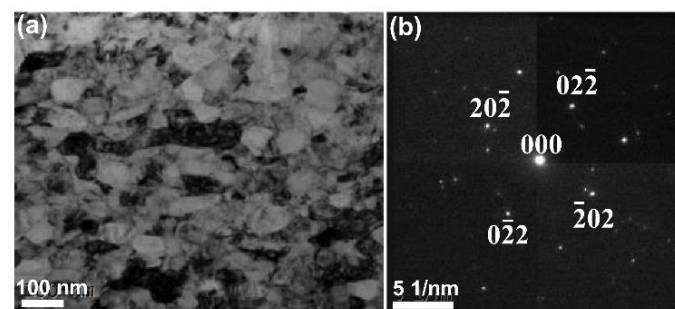

Figure 1. (**a**) Bright field TEM image and (**b**) selected-area electron diffraction (SAED) pattern of Monel 400 alloy.

3.2. Electrochemical Corrosion Behavior

Figure 2a shows the open circuit potential curves of the Monel 400 alloy under different rotational velocities. Before sliding, the OCP was stable at −0.23 V because of the presence of the passive film. With the onset of sliding, the OCP of the Monel 400 alloy dropped to −0.43 V at 0.125 m/s and further decreased to −0.45 V, −0.47 V and −0.50 V at 0.25 m/s, 0.375 m/s and 0.5 m/s, respectively. This result indicated that the passive film was damaged by mechanical wear and that the damage degree increased with the rotational velocity increasing. As the sliding proceeds, the OCP became stable with the achievement of an equilibrium between passivation and repassivation. When sliding stopped, the OCP value moved in the positive direction and eventually reached the initial potential of the Monel 400 alloy, indicating totally repassivation at the wear track. Figure 2b shows the Tafel

curves with and without sliding. Before sliding, the corrosion potential E_{corr} of Monel 400 alloy was determined to be -0.37 V. When sliding against the Al_2O_3 ceramic, the corrosion potential E_{corr} shifted to the negative direction. At 0.125 m/s, the corrosion potential was -0.45 V, which slowly decreased to -0.5 V as the rotational velocity increased to 0.5 m/s, indicating that the electrochemical corrosion of the Monel 400 alloy was promoted by mechanical wear.
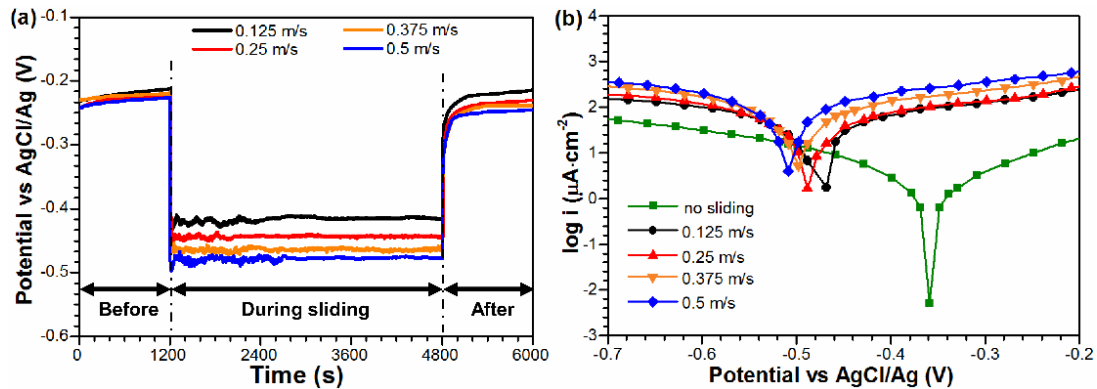

Figure 2. (**a**) Open circuit potential (OCP) curves and (**b**) Tafel curves under different rotational velocities in seawater.

3.3. Tribo-Corrosion Behavior

Figure 3 shows the total material loss rate and the friction coefficient under both tribo-corrosion- and mechanical-wear conditions at different rotational velocities. Generally, it was observed that the total material loss rate and friction coefficient under mechanical wear were larger than those under tribo-corrosion, which increased with the rotational velocity increasing under both conditions. Under tribo-corrosion conditions, the total material loss rate and friction coefficient of Monel 400 alloy were 31.8 mm/y and 0.32 at 0.125 m/s, respectively. As the rotational velocity increased to 0.5 m/s, the total material loss rate and friction coefficient of the Monel 400 alloy increased to 120.5 mm/y and 0.43, respectively. Similarly, under mechanical-wear conditions, when the rotational velocity increased from 0.125 m/s to 0.5 m/s, the material loss rate increased from 88.8 mm/y to 314.8 mm/y, and the friction coefficient increased from 0.35 to 0.45.
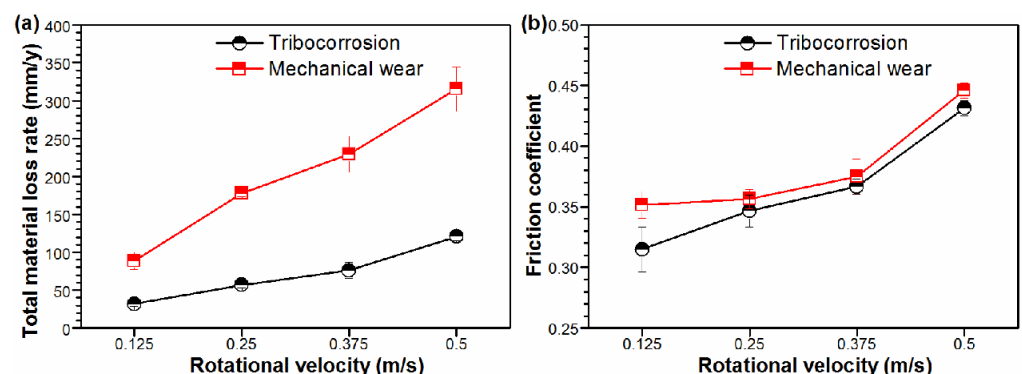

Figure 3. (**a**) Total material loss rate and (**b**) friction coefficient of Monel 400 alloy in seawater under both tribo-corrosion- and mechanical-wear conditions, with different rotational velocities ranging from 0.125 m/s to 0.5 m/s.

To evaluate the interaction between the corrosion and mechanical wear of the Monel 400 alloy in artificial seawater, extensive calculations were performed according to **ASTM G119-09**. The corresponding results are shown in Figure 4. From Figure 4a, as the rotational velocity increased from 0.125 m/s to 0.5 m/s, the total corrosion rate of the Monel 400 alloy

during tribo-corrosion slightly increased from 0.35 mm/y to 0.44 mm/y, which indicates accelerated electrochemical corrosion because of mechanical wear. Figure 4b shows the influence of corrosion on mechanical wear under the tribo-corrosion condition. Both the total wear rate and pure mechanical wear rate increased with the rotational velocity increasing, being 31.4 mm/y and 88.3 mm/y at 0.125 m/s and increasing to 120.0 mm/y and 314.8 mm/y at 0.5 m/s, respectively. However, the pure mechanical wear rate was larger than the total wear rate, suggesting that electrochemical corrosion has an antagonistic effect on mechanical wear. Since the corrosion rate was far less than the wear rate, the total material loss rate was determined by the wear rate W_0, and the interaction S between corrosion and mechanical wear was oriented by the degree of corrosion-inhibited wear ΔW_c, as shown in Figure 4c. It proves that there exists a negative synergy between corrosion and mechanical wear for the Monel 400 alloy, under various velocities.
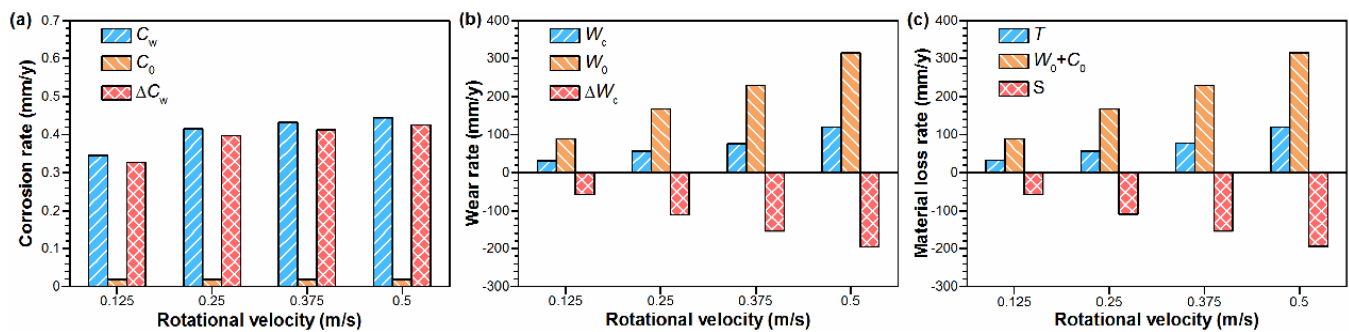

Figure 4. (a) The total corrosion rate (C_w), pure corrosion rate (C_0) and the change in corrosion caused by mechanical wear (ΔC_w); (b) total wear rate (W_c), mechanical wear rate (W_0) and the change in wear rate caused by corrosion (ΔW_c); and (c) the contribution of wear (W_0), corrosion (C_0) and mechanical wear-corrosion interaction (S) in total material loss rate (T), at different rotational velocities in seawater.

3.4. Damage Morphologies

Figure 5 shows the representative damaged surface of the Monel 400 alloy at different rotational velocities in seawater. It was noticed that the wear of Monel 400 alloy aggravated under both conditions, with the rotational velocity increasing. There were numerous parallel grooves together with flaky peelings on the damaged surface under tribo-corrosion- and mechanical-wear conditions, which was a typical characteristic of delamination wear and became more prominent at higher rotational velocities. Compared with the tribo-corrosion condition, the flaky peeling was more serious under mechanical wear at the same rotational velocity. For example, at 0.5 m/s, the dimensions of flaky peeling were 183 μm in length and 72 μm in width under tribo-corrosion conditions, which increased to 205 μm and 155 μm under independent mechanical wear, respectively. The damaged surface morphology observations partially explained why the total material loss rate was higher under the condition of mechanical wear, as shown in Figure 4c.

The cross-section morphologies of the Monel 400 alloy are presented in Figure 6. At 0.125 m/s, a few cracks were observed under tribo-corrosion conditions, while several voids were generated beneath the sliding surface under mechanical wear. With the rotational velocity increasing, cracks nucleated and propagated into the subsurface under the conditions of tribo-corrosion and mechanical wear. Compared with the tribo-corrosion conditions, the crack propagation was more serious under mechanical wear, presenting as a deeper damaged location and a larger area of the fractured region.
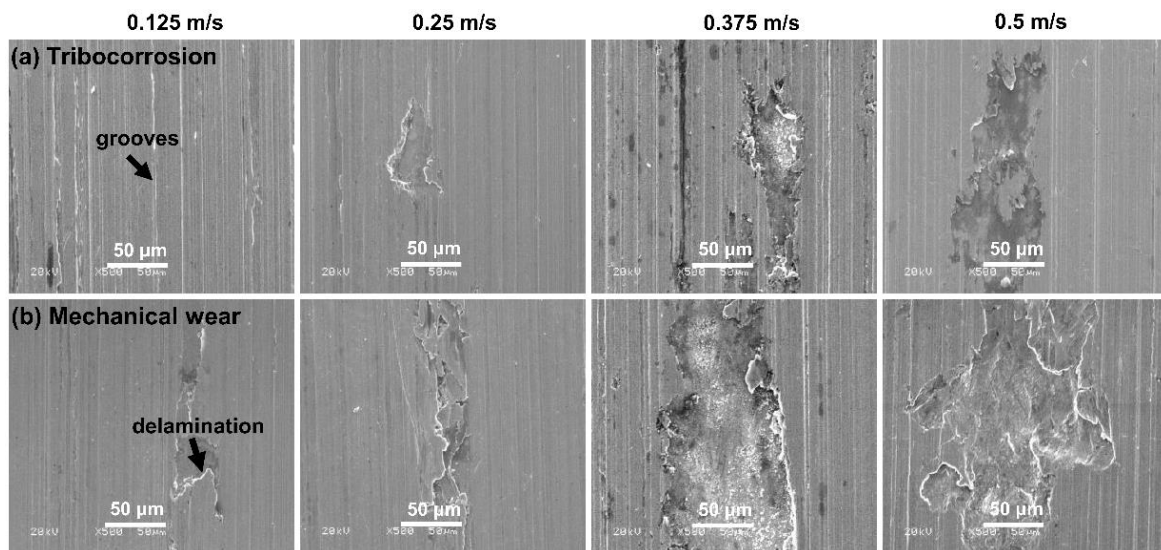
Figure 5. Damaged surface of Monel 400 alloy in conditions of (**a**) tribo-corrosion and (**b**) mechanical wear under different rotational velocities of 0.125 m/s, 0.25 m/s, 0.375 m/s and 0.5 m/s in seawater.

Figure 6. The cross-section morphologies of Monel 400 alloy in conditions of (**a**) tribo-corrosion and (**b**) mechanical wear under different rotational velocities of 0.125 m/s, 0.25 m/s, 0.375 m/s and 0.5 m/s in seawater.
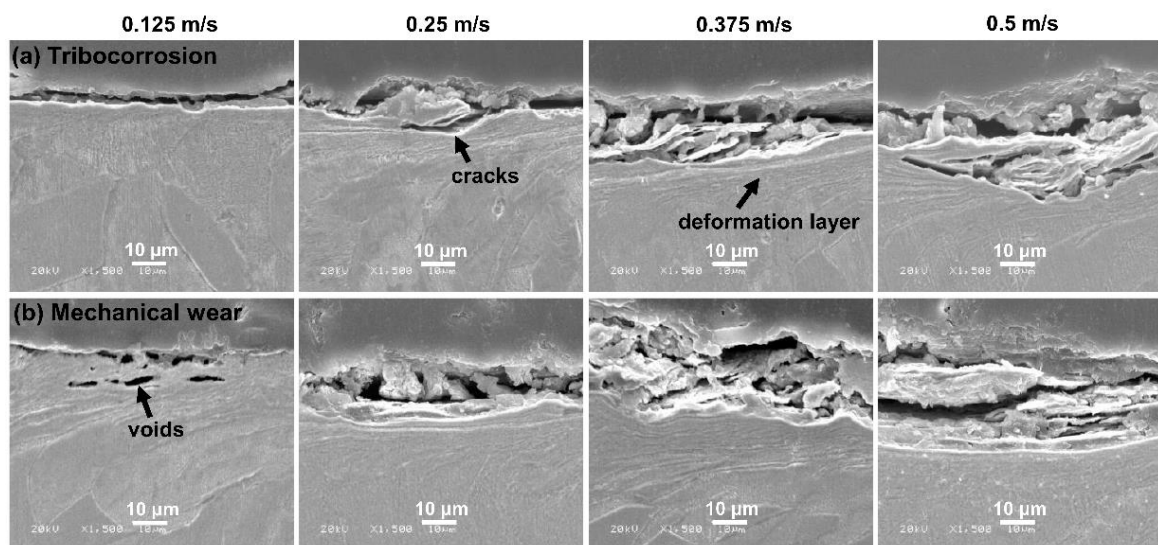
3.5. XPS Analysis of Corrosion Products

XPS analysis was conducted to reveal the chemical composition of corrosion products on the Monel 400 alloy under different conditions. Figure 7 presents the XPS spectrum of Ni 2p, Cu 2p and O 1s of the Monel 400 alloy at the original state and after the static corrosion and tribo-corrosion processes, respectively. The peak position, assignment and proportion are listed in Table 2. In the O1s spectrum, the peaks of O^{2-}, OH^- and O–C were located at 531.2 eV, 531.6 eV and 532.4 eV, respectively [23–25]. In the Ni $2p_{3/2}$ spectra, it was observed that the Ni species was the same under the three conditions. The peak of elemental Ni was detected at 852.3 eV, and the peaks located at 856.2 eV and 860.8 eV were indexed $Ni(OH)_2$ and its accompanying peak, respectively [26–28]. However, compared with the original state and static corrosion, the amount of Ni decreased to 4.1%, but the amount of $Ni(OH)_2$ increased to 61.1% after the tribo-corrosion tests. For the Cu $2p_{3/2}$ spectra, the binding energies of CuO and $Cu(OH)_2$ were 933.0 eV and 935.0 eV, respectively. The peak located at 932.1 eV belonged to elemental Cu or Cu_2O [29–31]. According to the

O1s spectra and the peak proportion listed in Table 3, it was deduced that Ni was oxidized to Ni(OH)$_2$ under both the static corrosion and tribo-corrosion conditions, while Cu(OH)$_2$ was generated after the corrosion process, together with a larger amount of Cu$_2$O.
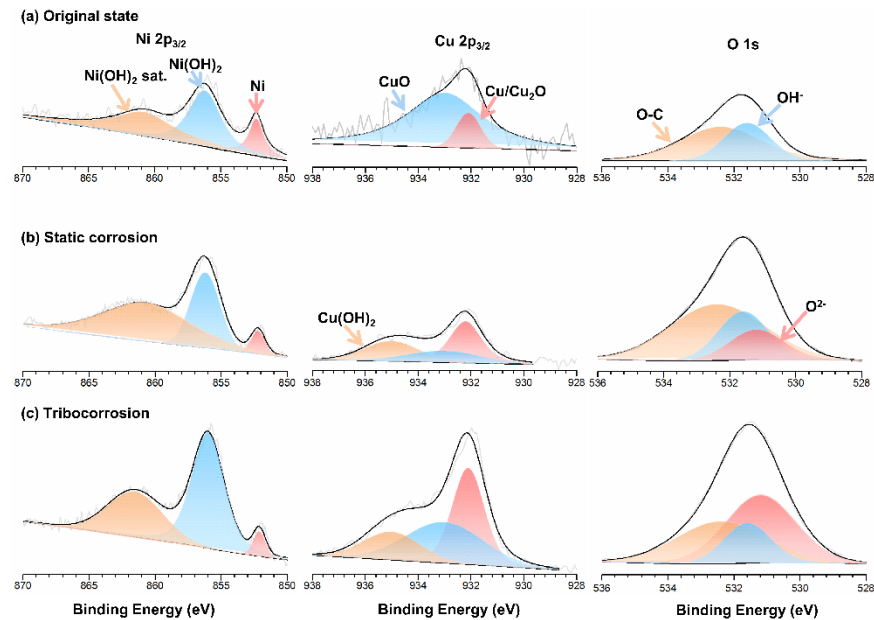

Figure 7. The XPS spectra of Ni 2p, Cu 2p and O 1s detected for corrosion products formed under the (**a**) original state, (**b**) static corrosion and (**c**) tribo-corrosion conditions.

Table 3. The assignment, binding energy and proportion of characteristic peaks from XPS analysis.

Samples		Ni 2p$_{3/2}$/Binding Energy/Amount			Cu 2p$_{3/2}$/Binding Energy/Amount			O 1s/Binding Energy/Amount		
Original State	Ni metal Ni(OH)$_2$	Main Sat.	852.3 856.2 860.8	15.5% 43.8% 40.7%	Cu/Cu$_2$O CuO Cu(OH)$_2$	932.1 933.0 /	12.9% 87.1% /	O^{2-} OH$^-$ O-C	/ 531.6 532.4	/ 36.9% 63.1%
Static Corrosion	Ni metal Ni(OH)$_2$	Main Sat.	852.3 856.2 860.8	5.2% 54.2% 40.6%	Cu/Cu$_2$O CuO Cu(OH)$_2$	932.1 933.0 935.0	45.5% 23.7% 30.8%	O^{2-} OH$^-$ O-C	531.2 531.6 532.4	17.1% 25.8% 57.1%
Tribo-Corrosion	Ni metal		852.3	4.1%	Cu/Cu$_2$O	932.1	41.7%	O^{2-}	531.2	46.1%
	Ni(OH)$_2$	Main Sat.	856.2 860.8	61.1% 34.8%	CuO Cu(OH)$_2$	933.0 935.0	38.7% 19.6%	OH$^-$ O–C	531.6 532.4	18.2% 35.7%

4. Discussion

4.1. Effect of Rotational Velocity on Mechanical Wear

The influence of rotational velocity on the microstructure after mechanical wear was explored by observing the subsurface morphologies of the Monel 400 alloy, and the typical TEM morphologies are presented in Figure 8. The rotational velocity had a significant effect on the microstructure of the subsurface. As can be seen from Figure 8a, compared with the original grain size of the Monel 400 alloy (~100 nm), the grain size of the Monel 400 alloy was significantly smaller (~25 nm) at the rotational velocity of 0.125 m/s, indicating that grain refinement occurred in the subsurface of the Monel 400 alloy after undergoing plastic deformation. However, at the rotational velocity of 0.5 m/s, the subsurface of the Monel 400 alloy exhibited extremely elongated grains, and fine grains only existed near the damaged surface.
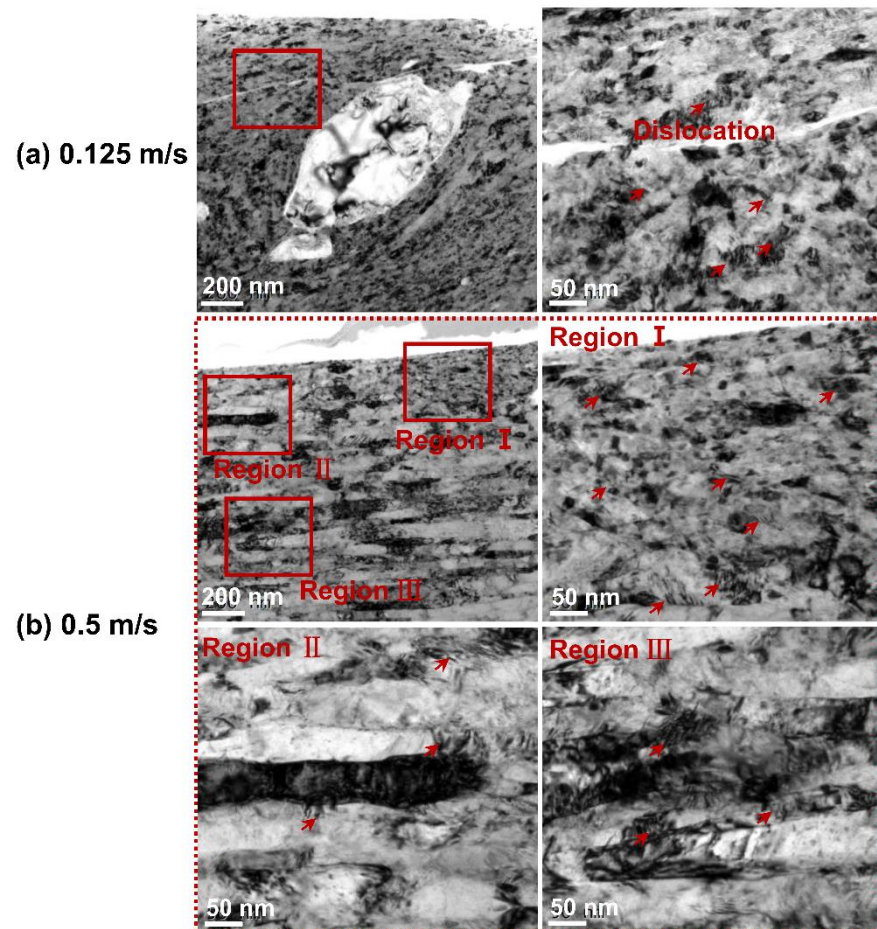
Figure 8. TEM morphologies of Monel 400 alloy after mechanical wear tests at (**a**) 0.125 m/s and (**b**) 0.5 m/s.

From the mechanical-wear perspective, the maximum contact stress was calculated as ~2.2 GPa based on the Hertz theory, as in spherical pin/ring contact, which is approximately 10 times larger than the yield stress of Monel 400 (typically 283 MPa). It means that the Monel 400 alloy would suffer severe plastic deformation under this condition. During the process of plastic deformation, part of the mechanical energy was stored in the metallic matrix, in the form of dislocation, with a medium value of the stacking fault energy of the Monel 400 alloy in the range of 80–128 mJ/m^2, even under the lubricating effect of seawater [32,33]. Firstly, under the action of shear stress, grain reorientation results in grain elongation in the shear direction. At the same time, there are many dislocations around the elongated grain boundary, and the slipping of dislocations caused by severe plastic deformation led to the rupture of the elongated grain. Next, the elongated grains were refined to form nanocrystalline [34,35]. At a higher rotational velocity, the wear is mainly controlled by plastic deformation peeling and fatigue fracture, which rapidly consumes the nanocrystalline layer on the surface. Therefore, at rotational velocity of 0.5 m/s, only a few refined grains were observed on the subsurface of the Monel 400 alloy.

In addition, from the quantitative measurement of tribo-corrosion components at various velocities shown in Figure 4, it was revealed that the total material loss (*T*) was mainly determined by the additive of mechanical wear (W_0) and corrosion-accelerated wear (ΔW_c). The exact values of *T*, W_0 and ΔW_c increased as the increasing velocity, and, thus, the sliding distance increased. However, as shown in Figure 9, it was revealed that the increased value of *T* and W_0, with the distance per cycle remaining constant, indicates that the microscopic accelerated wear loss at a higher velocity is mainly the result of

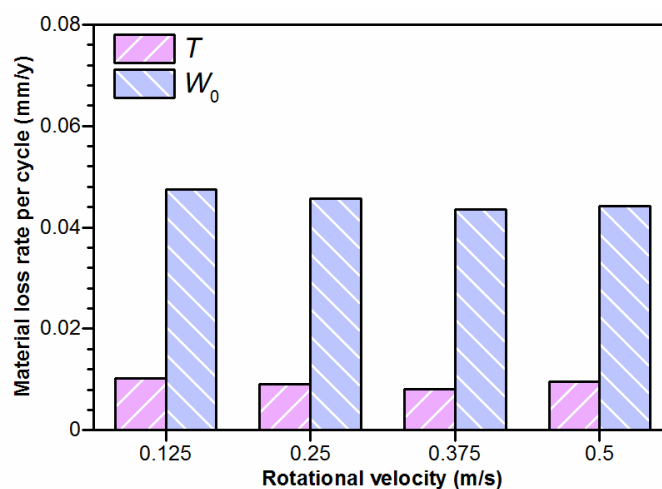the accumulation of the sliding distance, and elongated grains were observed at higher velocities.

Figure 9. The material loss rate per cycle after tribo-corrosion and mechanical wear at various rotational velocities.

4.2. Effect of Rotational Velocity on Corrosion

From the above results, it can be concluded that the corrosion of the Monel 400 alloy in artificial seawater inhibited the mechanical wear to different extents, which was mainly dependent on the excellent lubricating performance of the corrosion product's layer. According to our previous study [22], nanoscale copper-rich particles were produced *in situ* on the worn surface of the Monel 400 alloy, which was attributed to the selective corrosion of nickel during the tribo-corrosion tests. The copper-rich grains were extruded under cyclic shear stress and gradually evolved into a discontinuous corrosion product's layer. Owing to the excellent lubrication of the corrosion product's layer, the shear stress during the friction process was greatly weakened, leading to lower material loss and a lower friction coefficient after the tribo-corrosion tests than after the mechanical wear tests.

The tribo-corrosion behavior of the Monel 400 alloy was influenced remarkably by the rotational velocity. The material loss rate and friction coefficient after both tribo-corrosion and mechanical wear tests increased, with the rotational velocities ranging from 0.125 m/s to 0.5 m/s. Figure 10 depicts the TEM morphologies of the Monel 400 alloy after tribo-corrosion tests at 0.125 m/s and 0.5 m/s. The corrosion products' layer on the worn surface was observed. Spot-scanning results revealed that the chemical composition of the corrosion product's layer was mainly Cu, which was consistent with our previous research. However, the thickness of the corrosion product's layer decreased from 50 nm to 30 nm as the velocity increased from 0.125 m/s to 0.5 m/s. The evolution of the corrosion product's thickness was clearly controlled by the process of passivation and repassivation competition [36]. Mischler et al. observed the same behavior after tribo-corrosion tests, when AISI 430 steel sliding against an alumina ball was held at a passive potential in H_2SO_4 [37]. This evolution can be explained by the truth that the corrosion product's layer was continuously removed and exposed the matrix area where the corrosion took place at a higher rate when the rotational velocity increased [38], which is confirmed by Figure 4a. It can be observed that the degree of mechanical wear accelerated the increased corrosion (ΔC_w) with the velocity increasing, indicating that, although the thickness of the corrosion product's layer thinned with the rotational velocity increasing, it still allowed the Monel 400 alloy to completely repassivate, even at the maximum rotational velocity.
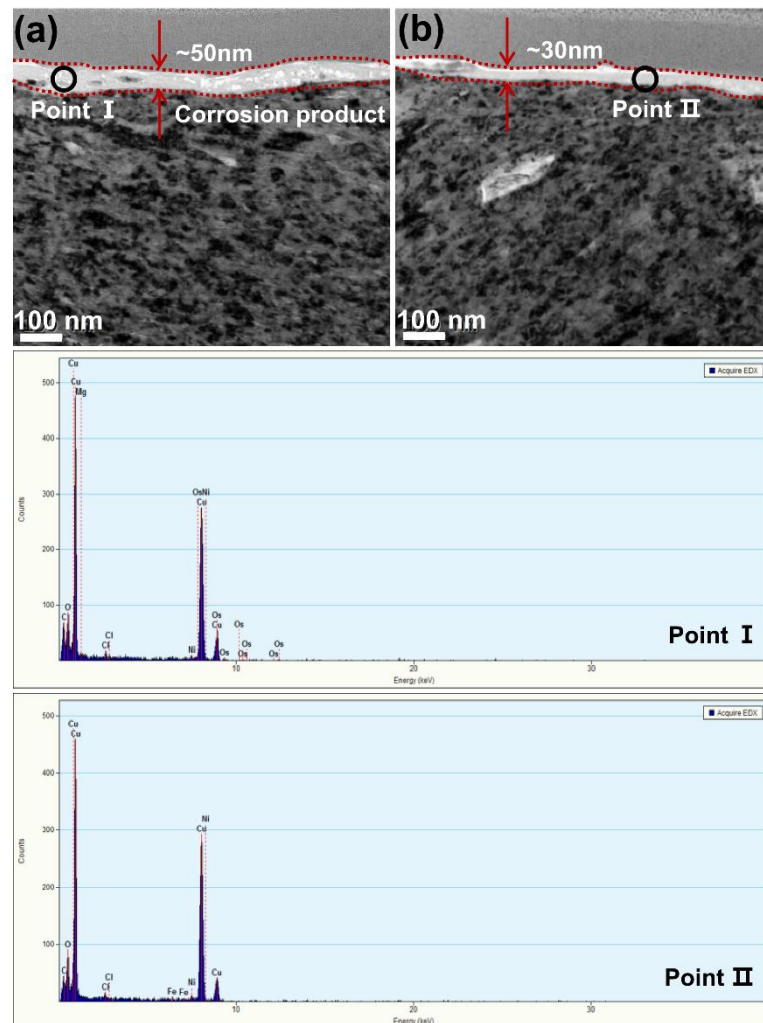
Figure 10. TEM images of the Monel 400 alloy and the chemical composition of corrosion product's layer after tribo-corrosion tests at (**a**) 0.125 m/s and (**b**) 0.5 m/s.

5. Conclusions

The influence of rotational velocities on the tribo-corrosion behavior of the Monel 400 alloy in artificial seawater was investigated. The components of mechanical wear, corrosion and wear-corrosion interaction were quantitatively determined. The results revealed that the tribo-corrosion behavior was highly dependent on the rotational velocity. The specific conclusions are listed as follows:

1. The total material loss and friction coefficient increased with the increasing velocity, presenting as delamination alongside the sliding direction at the surface and the crack nucleation and propagation at the subsurface.
2. Compared with mechanical wear, the damage induced by tribo-corrosion was much lower due to the formation of the corrosion product's layer in a thickness of several tens of nanometers, exhibiting excellent lubricating performance.
3. After the mechanical wear tests, the increased material loss rate with the increasing velocity was mainly the result of the accumulation of the sliding distance.
4. Since the thickness of the corrosion product's layer decreases from 50 nm to 30 nm as the velocity increases from 0.125 m/s to 0.5 m/s, the material loss rate after the tribo-corrosion tests also increases with the velocities increasing, possibly due to the rebuilt balance between the passivation and slowed repassivation at higher velocities.

References

1. Wang, C.; Wang, S.; Wang, H.; Ruan, G.; Xiao, Y.; Jiang, Z.; Li, X. Research status and prospects of tribological behaviors of key friction pairs of materials in marine equipment. *Mater. Sci.-Medzg.* **2021**, *27*, 148–154. [CrossRef]
2. Li, R.; Wen, C.; Meng, X.; Xie, Y. Measurement of the friction force of sliding friction pairs in low-speed marine diesel engines and comparison with numerical simulation. *Appl. Ocean. Res.* **2022**, *121*, 103089. [CrossRef]
3. Liang, Y.; Gao, D.; Chen, B.; Zhao, J. Friction and wear study on friction pairs with a biomimetic non-smooth surface of 316L relative to CF/PEEK under a seawater lubricated condition. *Chin. J. Mech. Eng.* **2019**, *32*, 66. [CrossRef]
4. Yuan, S.J.; Pehkonen, S.O. Surface characterization and corrosion behavior of 70/30 Cu-Ni alloy in pristine and sulfide-containing simulated seawater. *Corros. Sci.* **2007**, *49*, 1276–1304. [CrossRef]
5. Marenych, O.; Kostryzhev, A. Strengthening Mechanisms in Nickel-Copper Alloys: A Review. *Metals* **2020**, *10*, 1358. [CrossRef]
6. Jiang, W.; Zhu, S.; Wang, S. Effect of sliding speed and hardness on wear behavior and mechanism of AISI H13 steel. *Proc. Inst. Mech. Eng. Part J J. Eng. Tribol.* **2020**, *234*, 1822–1833. [CrossRef]
7. Mahmud, D.N.F.; Bin Abdollah, M.F.; Bin Masripan, N.A.; Tamaldin, N.; Amiruddin, H. Influence of contact pressure and sliding speed dependence on the tribological characteristics of an activated carbon-epoxy composite derived from palm kernel under dry sliding conditions. *Friction* **2019**, *7*, 227–236. [CrossRef]
8. Hedenqvist, P.; Olsson, M. Sliding Wear Testing of Coated Cutting-Tool Materials. *Tribol. Int.* **1991**, *24*, 143–150. [CrossRef]
9. Henry, P.; Takadoum, J.; Bercot, P. Depassivation of some metals by sliding friction. *Corros. Sci.* **2011**, *53*, 320–328. [CrossRef]
10. Chen, J.; Yan, F. Corrosive Wear Performance of Monel K500 Alloy in Artificial Seawater. *Tribol. Trans.* **2013**, *56*, 848–856. [CrossRef]
11. Mischler, S.; Debaud, S.; Landolt, D. Wear-accelerated corrosion of passive metals in tribocorrosion systems. *J. Electrochem. Soc.* **1998**, *145*, 750–758. [CrossRef]
12. Obadele, B.A.; Andrews, A.; Shongwe, M.B.; Olubambi, P.A. Tribocorrosion behaviours of AISI 310 and AISI 316 austenitic stainless steels in 3.5% NaCl solution. *Mater. Chem. Phys.* **2016**, *171*, 239–246. [CrossRef]
13. Xu, Y.D.; Qi, J.H.; Nutter, J.; Sharp, J.; Bai, M.W.; Ma, L.; Rainforth, W.M. Correlation between the formation of tribofilm and repassivation in biomedical titanium alloys during tribocorrosion. *Tribol. Int.* **2021**, *163*, 107147. [CrossRef]
14. Chen, H.; Zhang, Z.; Hao, X.H.; Huang, B.X.; Zhao, X.C.; Hu, C.C. Microstructure and tribocorrosion properties of NiTi/AlNi2Ti ternary intermetallic alloy. *Vacuum* **2021**, *184*, 109928. [CrossRef]
15. Kossman, S.; Coelho, L.B.; Mejias, A.; Montagne, A.; Van Gorp, A.; Coorevits, T.; Touzin, M.; Poorteman, M.; Olivier, M.G.; Iost, A.; et al. Impact of industrially applied surface finishing processes on tribocorrosion performance of 316L stainless steel. *Wear* **2020**, *456*, 203341. [CrossRef]
16. Ziomek-Moroz, M.; Miller, A.; Hawk, J.; Cadien, K.; Li, D.Y. An overview of corrosion-wear interaction for planarizing metallic thin films. *Wear* **2003**, *255*, 869–874. [CrossRef]
17. Liu, M.; Wang, Z.G.; Shi, C.B.; Wang, L.W.; Xue, X.D. Corrosion and wear behavior of Ti-30Zr alloy for dental implants. *Mater. Res. Express* **2019**, *6*, 0865c8. [CrossRef]
18. Namus, R.; Nutter, J.; Qi, J.; Rainforth, W.M. Sliding speed influence on the tribo-corrosion behaviour of Ti6Al4V alloy in simulated body fluid. *Tribol. Int.* **2021**, *160*, 107023. [CrossRef]
19. Bi, Q.; Liu, W.; Ma, J.; Yang, J.; Pu, Y.; Xue, Q. Tribocorrosion behavior of Ni-17.5Si-29.3Cr alloy in sulfuric acid solution. *Tribol. Int.* **2009**, *42*, 1081–1087. [CrossRef]
20. Ferreira, D.F.; Ale Almeida, S.M.; Soares, R.B.; Juliani, L.; Bracarense, A.Q.; Cunha Lins, V.d.F.; Rabelo Junqueira, R.M. Synergism between mechanical wear and corrosion on tribocorrosion of a titanium alloy in a Ringer solution. *J. Mater. Res. Technol.* **2019**, *8*, 1593–1600. [CrossRef]
21. Zhu, Y.; Liu, H.; Zhang, D.; Wang, J.; Yan, F. Effect of polarization potentials on tribocorrosion behavior of Monel 400 alloy in seawater environment. *Tribol. Int.* **2022**, *168*, 107445. [CrossRef]
22. Zhu, Y.H.; Liu, H.; Wang, J.Z.; Yan, F.Y. Antagonistic effect of electrochemical corrosion on the mechanical wear of Monel 400 alloy in seawater. *Corros. Sci.* **2022**, *198*, 110120. [CrossRef]
23. Ayiania, M.; Smith, M.; Hensley, A.J.R.; Scudiero, L.; McEwen, J.-S.; Garcia-Perez, M. Deconvoluting the XPS spectra for nitrogen-doped chars: An analysis from first principles. *Carbon* **2020**, *162*, 528–544. [CrossRef]

24. Lee, E.; Lee, C.E.; Han, J.H. Effects of proton irradiation on single-stranded DNA studied by using X-ray photoelectron spectroscopy. *J. Korean Phys. Soc.* **2016**, *69*, 578–583. [CrossRef]

25. Okada, K.; Kotani, A. Oxygen is core-level photoemission as a tool to investigate the unoccupied electronic states of cuprates. *J. Phys. Soc. Jpn.* **2006**, *75*, 123703. [CrossRef]

26. Chen, W.; Chu, M.; Gao, L.; Mao, L.; Yuan, J.; Shangguan, W. Ni(OH)(2) loaded on TaON for enhancing photocatalytic water splitting activity under visible light irradiation. *Appl. Surf. Sci.* **2015**, *324*, 432–437. [CrossRef]

27. Jeong, D.J.; Kim, W.S.; Choi, Y.K.; Sung, Y.E. Intercalation/deinterealation characteristics of electrodeposited and anodized nickel thin film on ITO electrode in aqueous and nonaqueous electrolytes. *J. Electroanal. Chem.* **2001**, *511*, 79–87. [CrossRef]

28. Wang, W.; Wang, W.; Wang, M.; Guo, X. Facile In Situ Synthesis of Hierarchical Porous Ni/Ni(OH)(2) Hybrid Sponges with Excellent Electrochemical Energy-Storage Performances for Supercapacitors. *Chem. Asian J.* **2014**, *9*, 2590–2596. [CrossRef]

29. Tao, Z.; Gu, J.; Fang, H.; Chen, L.; Chen, J. Cu doped epsilon-Fe2-3N films with manipulable magnetic and transport properties. *Mater. Lett.* **2019**, *250*, 131–134. [CrossRef]

30. Arun, L.; Karthikeyan, C.; Philip, D.; Sasikumar, M.; Elanthamilan, E.; Merlin, J.P.; Unni, C. Effect of Ni^{2+} doping on chemocatalytic and supercapacitor performance of biosynthesized nanostructured CuO. *J. Mater. Sci.-Mater. Electron.* **2018**, *29*, 21180–21193. [CrossRef]

31. Pinon-Espitia, M.; Lardizabal-Gutierrez, D.; Camacho-Rios, M.L.; Herrera-Perez, G.; Ochoa-Lara, M.T. Electronic structure comparison of Cu 2p and O 1s X-Ray photoelectron spectra for CuxO nanofibers (x = 1, 2, i). *Mater. Chem. Phys.* **2021**, *272*, 124981. [CrossRef]

32. Hansen, N.; Jensen, D.J. Development of microstructure in FCC metals during cold work. *Philos. Trans. R. Soc. A-Math. Phys. Eng. Sci.* **1999**, *357*, 1447–1469. [CrossRef]

33. Ebrahimi, G.R.; Momeni, A.; Ezatpour, H.R.; Jahazi, M.; Bocher, P. Dynamic recrystallization in Mone1400 Ni-Cu alloy: Mechanism and role of twinning. *Mater. Sci. Eng. A-Struct. Mater. Prop. Microstruct. Process.* **2019**, *744*, 376–385. [CrossRef]

34. Singh, J.B.; Cai, W.; Bellon, P. Dry sliding of Cu-15 wt%Ni-8 wt%Sn bronze: Wear behaviour and micro structures. *Wear* **2007**, *263*, 830–841. [CrossRef]

35. Roncery, L.M.; Jacome, L.A.; Aghajani, A.; Theisen, W.; Weber, S. Subsurface characterization of high-strength high-interstitial austenitic steels after impact wear. *Wear* **2018**, *402*, 137–147. [CrossRef]

36. Stemp, M.; Mischler, S.; Landolt, D. The effect of mechanical and electrochemical parameters on the tribocorrosion rate of stainless steel in sulphuric acid. *Wear* **2003**, *255*, 466–475. [CrossRef]

37. Mischler, S. Triboelectrochemical techniques and interpretation methods in tribocorrosion: A comparative evaluation. *Tribol. Int.* **2008**, *41*, 573–583. [CrossRef]

38. Benea, L.; Ponthiaux, P.; Wenger, F.; Galland, J.; Hertz, D.; Malo, J.Y. Tribocorrosion of stellite 6 in sulphuric acid medium: Electrochemical behaviour and wear. *Wear* **2004**, *256*, 948–953. [CrossRef]